









High-temperature capacitive energy storage in polymer nanocomposites through nanoconfinement

Received: 20 June 2024

Accepted: 25 July 2024

Published online: 06 August 2024

 Check for updates

Xinhui Li¹, Bo Liu¹, Jian Wang¹, Shuxuan Li¹, Xin Zhen¹, Jiapeng Zhi¹, Junjie Zou¹, Bei Li¹ , Zhonghui Shen¹ , Xin Zhang¹  , Shujun Zhang²   & Ce-Wen Nan³  

Polymeric-based dielectric materials hold great potential as energy storage media in electrostatic capacitors. However, the inferior thermal resistance of polymers leads to severely degraded dielectric energy storage capabilities at elevated temperatures, limiting their applications in harsh environments. Here we present a flexible laminated polymer nanocomposite where the polymer component is confined at the nanoscale, achieving improved thermal-mechanical-electrical stability within the resulting nanocomposite. The nanolaminate, consisting of nanoconfined polyetherimide (PEI) polymer sandwiched between solid Al₂O₃ layers, exhibits a high energy density of 18.9 J/cm³ with a high energy efficiency of ~91% at elevated temperature of 200°C. Our work demonstrates that nanoconfinement of PEI polymer results in reduced diffusion coefficient and constrained thermal dynamics, leading to a remarkable increase of 37°C in glass-transition temperature compared to bulk PEI polymer. The combined effects of nanoconfinement and interfacial trapping within the nanolaminates synergistically contribute to improved electrical breakdown strength and enhanced energy storage performance across temperature range up to 250°C. By utilizing the flexible ultrathin nanolaminate on curved surfaces such as thin metal wires, we introduce an innovative concept that enables the creation of a highly efficient and compact metal-wired capacitor, achieving substantial capacitance despite the minimal device volume.

Dielectric energy storage capacitors with ultrafast charging-discharging rates are indispensable for the development of the electronics industry and electric power systems^{1–3}. However, their low energy density compared to electrochemical energy storage devices fails to meet the requirement of miniaturized and compact systems^{4–6}. On the other hand, the emerging harsh-condition-related industries, including downhole oil and gas exploration, hybrid electric vehicles,

and electrified aircraft, have generated a pressing requirement for dielectric capacitors capable of serving at a high temperature up to 200°C^{7–10}. Thus, it is imperative to develop dielectric materials characterized by both high energy storage capability and high-temperature stability.

The electrical energy storage of dielectrics relies on the application of an external electric field (E) on the dielectric layer to generate

¹State Key Laboratory of Advanced Technology for Materials Synthesis and Processing, Center of Smart Materials and Devices & International School of Materials Science and Engineering, Wuhan University of Technology, Wuhan 430070, China. ²Institute for Superconducting and Electronic Materials, Faculty of Engineering and Information Sciences, University of Wollongong, North Wollongong, NSW 2522, Australia. ³School of Materials Science and Engineering, State Key Lab of New Ceramics and Fine Processing, Tsinghua University, Beijing 100084, China. ✉ e-mail: zhang-xin@whut.edu.cn; shujun@uow.edu.au; cwnan@tsinghua.edu.cn

an electrical displacement (D , $D = \epsilon_0 \epsilon_r E$, ϵ_0 and ϵ_r are the vacuum dielectric permittivity and relative dielectric permittivity of the dielectrics, respectively), and the energy density (U_e) of the linear dielectrics can be calculated as $U_e = \frac{1}{2} \epsilon_0 \epsilon_r E_b^2$. Therefore, high breakdown strength (E_b , the highest electric field that materials can withstand) and high ϵ_r are expected to achieve a high U_e , where a high E_b is of particular significance due to its quadratic dependence. Conventional ceramic dielectrics can withstand a high serving temperature up to a few hundred degrees Celsius, but suffer inflexibility and a mediocre E_b . So far, there have been no reports on flexible ceramic dielectrics for electrostatic energy storage applications. In contrast, polymeric dielectrics have advantages in terms of inherent flexibility, high E_b , and easy processing^{11,12}. Unfortunately, the current commercially available polymer film represented by biaxially oriented polypropylene (BOPP) film can only withstand temperatures below 85 °C¹³. Despite the exploration of engineering polymers with high glass-transition temperature (T_g), such as polyetherimide (PEI) and polyimide (PI), to enable operation at higher temperatures, these materials still experience a thermal-induced degradation in electrical insulation and mechanical strength when subjected to elevated temperatures¹⁴. As a consequence, this leads to a deteriorated E_b , excessive conduction loss, and limited U_e .

To improve the high-temperature energy storage performance of dielectric polymers, efforts have been devoted to developing polymer nanocomposites with nanoreinforcements¹⁵. On one hand, inorganic nanofillers such as boron nitride and Al_2O_3 , which possess high thermal conductivity and large bandgap, are incorporated into the polymer matrix or applied to the polymer surfaces to enhance thermal dissipation and electrical insulation at elevated temperatures^{16–18}. On the other hand, the parallel all-organic nanocomposites are fabricated by incorporating high-electron-affinity molecular fillers, constructing blends, and establishing crosslinking structures to suppress electrical conduction while stabilizing charge transport^{19–22}. Despite some progress through these strategies, current polymer-based dielectric materials still exhibit a low U_e of $\sim 7 \text{ J/cm}^3$ (with an energy efficiency of $>90\%$) at a temperature of 200 °C^{1,10,23,24}. There remains an ongoing urgency to augment the high-temperature energy density further, aiming to broaden the scope of potential applications.

In prior polymer nanocomposites, the incorporation of nanoscale organic/inorganic reinforcements has alleviated the conduction loss and thermal runaway occurring at high temperatures. However, the inherent inferiority in thermal stability of the host polymers remains unaddressed, hindering the advancement of energy storage performance at elevated temperatures. It is generally believed that the molecular structures of polymers undergo changes as they approach the solid surfaces. This will induce altered dynamics and a distinct glass-transition temperature (T_g) for ultrathin polymer films that are adsorbed onto solid surfaces, in contrast to bulk polymers^{25–28}. Polymer thin films with free surfaces exhibit a decreased T_g ²⁹, however, when the surfaces of polymer thin film are wetted, the T_g can increase due to the confinement effects³⁰. Here we propose that the controllable thermal dynamics through nanoconfinement in ultrathin polymer films hold great promise for improving the thermal stability and high-temperature energy storage properties of polymer dielectrics.

Here, we demonstrate the development of flexible laminated polymer/ceramic nanocomposites wherein the polymer component is confined at the nanoscale. This approach leads to an enhanced thermal stability of the polymers, thereby improving energy storage properties at elevated temperatures in the resulting nanolaminate. This strategic methodology is applicable to general polymer/ceramic composites, encompassing readily available, cost-effective, and industrially reliable materials such as PEI and Al_2O_3 . As exemplified in this work, a flexible laminated nanocomposite was prepared by confining soft PEI ultrathin polymer films between Al_2O_3 layers. By employing molecular dynamic

simulations and modified probe-based in-situ measurements, we demonstrate that the thermal dynamics of PEI undergo alterations in the vicinity of the Al_2O_3 surface, which improves its thermal stability, leading to simultaneous improvements in high-temperature mechanical strength and electrical insulation. Notably, the T_g of the 10-nm-thick nanoconfined PEI ultrathin film is increased by ~ 37 °C compared to bulk PEI polymer. The enhanced thermal-mechanical-electrical stability of PEI ultrathin film endows greatly improved breakdown strength to the PEI- Al_2O_3 nanolaminate at elevated temperatures. In particular, the thermal-electrical stability and breakdown strength can be further improved by fabricating PEI- Al_2O_3 multilayered nanolaminate, utilizing multiple interfaces. Consequently, the resulting flexible PEI- Al_2O_3 nanolaminate exhibits a high U_e , with values of 24.0 J/cm^3 at 150 °C and 18.9 J/cm^3 at 200 °C, even 3.9 J/cm^3 at 250 °C. Of particular importance is that a high energy efficiency of $>90\%$ is maintained over the entire temperature range from 25 to 250 °C.

Results

Nanoconfined PEI polymers by Al_2O_3 solid surfaces

For the preparation of PEI- Al_2O_3 nanolaminates, a bottom Al_2O_3 nanolayer was first deposited using plasma-enhanced atomic layer deposition (ALD), the PEI thin films with varying thickness were then attached to the bottom Al_2O_3 layer by a solution-based spinning-coating process (Supplementary Figs. 1, 2), and followed by the deposition of an upper Al_2O_3 nanolayer. The Al_2O_3 nanolayers, renowned for their excellent insulating properties, serve a dual role in the polymer-ceramic nanolaminate, i.e., providing a solid surface for confining PEI polymer while also acting as an inorganic reinforcement. The trilayered PEI- Al_2O_3 nanolaminate was annealed at 250 °C to cure the PEI/ Al_2O_3 interfaces and fully wet the surfaces of the PEI thin films with the ceramic layer Al_2O_3 . To explore the impact of nanoconfinement, we first performed a molecular dynamics simulation of the molecular structures and thermal dynamics of PEI polymer wetted by Al_2O_3 . The binding energy between Al_2O_3 and PEI is determined to be $1.1 \text{ kcal}/(\text{mol} \cdot \text{Å}^2)$ (Supplementary Fig. 3), signifying the formation of a stable Al_2O_3 /PEI interface^{31,32}. The diffusion coefficient (D) of PEI polymer chains located at different positions was calculated to illustrate their dynamic behavior³³, as shown in Fig. 1a. The findings confirm that the PEI polymer in close proximity to the Al_2O_3 surface exhibits a lower D compared to those locations farther from the surface. Additionally, as expected, a higher chain packing density of PEI polymer is observed near the surface, due to the interactions between the PEI polymer and the Al_2O_3 surface (Supplementary Fig. 4)²⁵. With increasing temperatures, the D of PEI chains near the surface experiences a modest elevation, in contrast, an increase is observed in the central bulk PEI (Fig. 1b). For a more detailed visualization of molecular level changes in the dynamics of PEI polymer, Supplementary Fig. 5 illustrates the dynamic trajectory of C and O atoms from three distinct PEI chains located at different positions, i.e., near the top Al_2O_3 surface (Position 1), central region (Position 5), and close to the bottom Al_2O_3 surface (Position 10), as a function of temperature. Compared to the central bulk PEI, the trajectory range of C and O atoms near the surfaces is constrained, indicating remarkable confinement of mobility and dynamics for PEI polymer chains in close proximity to Al_2O_3 surfaces. This confirms the existence of nanoconfinement resulting from the interactions between PEI polymer and Al_2O_3 surface, as well as the possible stereo-hindrance from the solid surface that constrains group motion. With increasing temperature, the central atoms undergo a more pronounced expansion of their trajectory range compared to the surface atoms. Notably, at 200 °C, the surface atoms exhibit a trajectory range comparable to that of central atoms at 25 °C, highlighting the superior thermal stability of nanoconfined PEI polymer in close proximity to the Al_2O_3 surface.

The altered thermal dynamics of PEI near the Al_2O_3 surface are expected to play a dominant role in the properties of the confined PEI

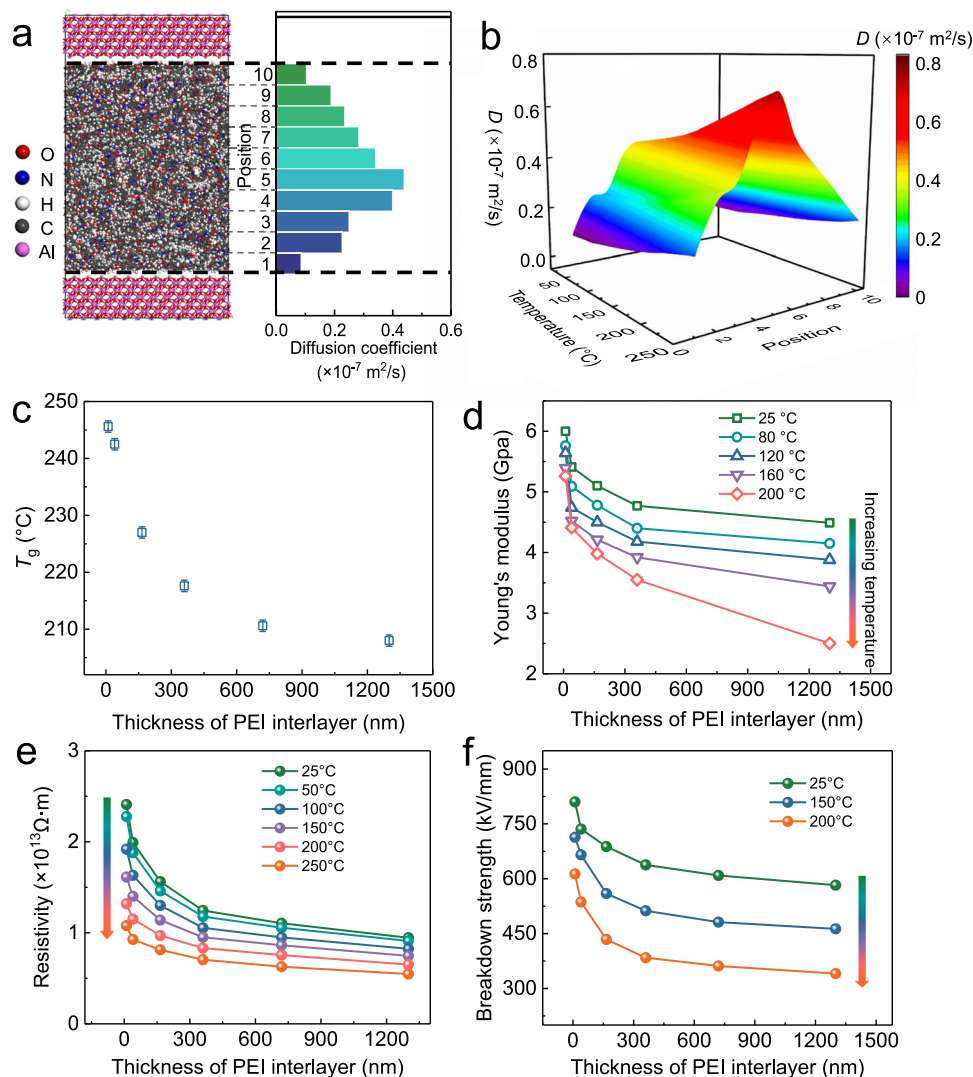


Fig. 1 | Molecular thermal dynamics and properties of nanoconfined PEI polymer wetted by Al_2O_3 . **a** The model constructed for molecular dynamic simulations featuring PEI polymer wetted by Al_2O_3 layers (left), and the corresponding diffusion coefficient (D) of PEI polymer chains at different positions from the bottom to top Al_2O_3 surfaces. **b** The diffusion coefficient of PEI polymer chains as a function of temperature. **c** Variation of T_g for confined PEI with different film thicknesses, the thickness of the Al_2O_3 layers is fixed at 28 nm. The error bars (± 1 °C) represent the

inherent error due to the fitting of the data required to obtain T_g . **d, e** Variations of **d** Young's modulus and **e** resistivity for PEI- Al_2O_3 nanolaminates with different PEI thicknesses at various temperatures, the thickness of the Al_2O_3 layers is fixed at 28 nm. **f** Dependency of breakdown strength on PEI film thickness for PEI- Al_2O_3 nanolaminates at various temperatures, the thickness of the Al_2O_3 layers is fixed at 28 nm.

ultrathin films, resulting in an enhancement in thermal stability. The T_g of the PEI thin films was measured by in-situ atomic force microscopy (AFM). As shown in Supplementary Fig. 6, the polymer film typically undergoes deformation when the temperature exceeds T_g , which can be detected by the atomic force probe based on a position-sensitive photodetector. The T_g of the PEI thin film confined between Al_2O_3 layers was measured and given in Fig. 1c and Supplementary Fig. 7. The T_g of PEI film with a thickness of 1.3 μm is determined to be 208 °C, similar to the T_g of bulk PEI polymer previously reported³⁴, confirming the validity and accuracy of the probe-based measurement method. With reducing the film thickness, the T_g increases progressively and reaches 245 °C for 10 nm PEI, which represents an increment of 37 °C compared to the bulk value. It is noteworthy that the 10 nm PEI, when confined by Al_2O_3 layers of various thicknesses, exhibits a comparable T_g (Supplementary Fig. 8). This suggests that the nanoconfinement effect on the thermal dynamics of PEI primarily arises from the inherent surface properties of Al_2O_3 and is minimally influenced by the thickness of these layers.

The enhanced thermal stability of PEI polymer under nanoconfinement is expected to endow PEI films with improved mechanical and electrical insulation properties, particularly at elevated temperatures. Young's modulus of the nanoconfined PEI thin films at different temperatures was further measured by AFM. The methodology for measuring Young's modulus is illustrated in the schematic diagram presented in Supplementary Fig. 9. Force curves from both the "Approach" and "Retract" stages were recorded to reveal the interaction between the AFM tip and the sample, measuring intra-/intermolecular forces and sample mechanics^{35–37}.

Figure 1d and Supplementary Fig. 10 present the obtained Young's modulus of PEI films with different thicknesses. It shows that Young's modulus of PEI progressively increases with the reduction of the thickness of PEI film. As an example, Young's modulus initially experiences a modest increase from 4.5 GPa in 1.3 μm PEI to 4.8 GPa in 320 nm PEI, and then undergoes a dramatic increase up to 6.0 GPa in 10 nm PEI. It can be observed that there is a gradual decrease in Young's modulus as the temperature increases, followed by a decline

once the T_g is reached (Supplementary Fig. 10). Despite this, the PEI ultrathin film consistently exhibits a greater Young's modulus compared to the thicker ones. Additionally, the ultrathin PEI film shows a stronger thermal-mechanical resistance to temperature elevation compared to the thicker PEI film. This can be evidenced by the Young's modulus of 1.3 μm PEI shows a 44% drop, while a milder 12% drop is observed for 10 nm PEI with increasing temperature from 25 to 200 °C. Alongside the improved thermal-mechanical stability, reducing the PEI film thickness also leads to enhanced electrical insulation. As shown in Fig. 1e, the overall resistivity of the laminates continuously increases by decreasing the thickness of PEI layer, the thickness-induced increment in resistivity is evident across the temperature range of 20 to 250 °C. This enhancement may be ascribed to a lower D in the ultrathin PEI film, which constrains the movement of chain groups and hinders charge carrier transport, particularly those ionic carriers associated with chain segment motion.

It is generally believed that the breakdown behavior of polymers greatly depends on their mechanical and electrical properties. The electromechanical breakdown of polymers, for instance, is determined by the mechanical endurance of the applied electrostatic force^{38,39}. In contrast, the thermal breakdown of polymers is related to the current-induced heat accumulation^{40,41}. Given the simultaneously improved mechanical and electrical insulation of PEI ultrathin films, considerably enhanced breakdown strengths of the PEI- Al_2O_3 laminates are expected at elevated temperatures. The breakdown strength of PEI- Al_2O_3 laminates with different PEI film thicknesses was analyzed by a two-parameter Weibull distribution function: $P(E) = 1 - \exp(-(E/E_b)^\beta)$, where $P(E)$ is the cumulative probability of the electric failure, E is the experimental breakdown strength, the scale parameter E_b is the characteristic breakdown strength corresponding to a 63.2% probability of failure. The shape parameter β is the Weibull modulus which represents the dispersion of E data and the quality of the film dielectrics⁴². The fitting results of PEI- Al_2O_3 laminates are given in Supplementary Fig. 11. The characteristic breakdown strengths of the PEI- Al_2O_3 laminates with different PEI film thicknesses over temperature range up to 200 °C are compared in Fig. 1f. At 25 °C, the E_b of PEI- Al_2O_3 laminate is progressively increased from 580 kV/mm for 1.3 μm PEI film to 810 kV/mm for 10 nm PEI. Despite the decrease in E_b with increasing temperature, the PEI- Al_2O_3 laminate with 10 nm PEI always demonstrates the highest E_b , which retains a high E_b value of 610 kV/mm at 200 °C, even superior to the room temperature value of 1.3 μm PEI film. It is important to note that the reduction of Al_2O_3 thickness to a specific value can impact the breakdown performance of the nanolaminate with 10 nm PEI. For instance, the E_b of the nanolaminates remains consistently within an Al_2O_3 thickness range of 28 to 98 nm but experiences a decline when the thickness is reduced to 14 nm (Supplementary Fig. 12). These observed breakdown dependencies on thickness could be attributed to tunneling effects⁴³. Therefore, maintaining an adequate Al_2O_3 thickness in multilayered nanolaminates is crucial for ensuring sufficient overall thickness and preventing tunneling current.

In addition to the enhanced breakdown strength, the overall dielectric constant of the trilayered PEI/ Al_2O_3 nanolaminate consistently increases as the thickness of the PEI film decreases, as illustrated in Supplementary Fig 13. This increase is firstly ascribed to a smaller PEI thickness resulting in a higher proportion of Al_2O_3 , which has an inherently higher ϵ_r of 10 compared to PEI (~3.2). Furthermore, we have determined the equivalent dielectric constant of the central PEI film using the series mixture law, revealing an increase in dielectric constant as the film thickness decreases, resulting in an enhanced value of ~4.5 for a 10-nm-thick PEI film (Supplementary Fig. 14). This increase in the dielectric constant of PEI is attributed to the interfacial effect between Al_2O_3 and PEI, which facilitates the formation of polar conformations in the PEI polymer⁴⁴. Additionally, despite the confined mobility of the PEI chain, the polar side groups, i.e., carbonyl groups,

still demonstrate favorable rotational mobility to maintain their dielectric response capability. This is evidenced by a comprehensive analysis of the trajectories of two distinct oxygen atoms within the same PEI chain. As depicted in Supplementary Fig. 15, the trajectory range of carbonyl oxygen atoms is greater than that of ether oxygen atoms due to superimposed rotational movements. This distinction in trajectories between these two oxygen atoms is observed across all PEI chains from various positions shown in Fig. 1a.

Multilayered PEI- Al_2O_3 nanolaminates and the impact of interface

The polymer/ceramic interfaces usually serve as traps, modulate the charge trapping and transport behaviors, presenting opportunities to enhance the electrical behaviors⁴⁵. To further improve the thermal-electrical stability of the laminate by creating multi-interfaces, we extended our endeavors by fabricating Al_2O_3 -PEI multilayered nanolaminate with several nanoconfined 10 nm PEI film layers beyond the 3-layered nanolaminate. Specifically, we fabricated a 5-layered nanolaminate containing two PEI nanofilms and a 7-layered nanolaminate containing three PEI nanofilms, which were designed to generate more interfaces between PEI and Al_2O_3 layers. The cross-sectional SEM images of these precisely controlled multilayered nanolaminates are shown in Fig. 2a and Supplementary Fig. 16. As observed, the PEI thickness is controlled at 10 nm, and the thickness of Al_2O_3 layers is varied to achieve an overall thickness of ~66 nm for the different multilayered nanolaminates. Supplementary Fig. 17 shows that the resistivity of the nanolaminates is further enhanced by increasing the number of layers, leading to the highest resistivity for 7-layered nanolaminate. Of particular importance is that, in contrast to the 3-layered nanolaminate, the resistivity of 7-layered nanolaminate exhibits a mild decrease with increasing temperature from 25 to 250 °C, highlighting an enhanced thermal-electrical stability.

The multilayered nanolaminates with more PEI/ Al_2O_3 interfaces also deliver suppressed leakage current density under high electric field. As shown in Supplementary Fig. 18, the leakage current densities of the nanolaminates typically remain at a low level of 10^{-6} A/cm² at an electric field of 300 kV/mm, where the 7-layered nanolaminate exhibits the lowest leakage current density with minimal variation over the temperature range from 25 to 200 °C. The fitting of the leakage current density versus electric field at 150 and 200 °C demonstrates that the electrical conduction behaviors of the nanolaminate are predominantly governed by a charge injection-controlled Schottky emission mechanism at low fields, while exhibiting a hopping conduction mechanism at higher fields (Fig. 2b and Supplementary Figs. 19–22). The increase in the number of layers leads to a reduction in the intercept of the Schottky emission fitting results (Supplementary Fig. 20), indicating an enhanced electrode/dielectric interfacial barrier in 7-layered and 5-layered nanolaminates compared to the 3-layered nanolaminate⁴⁶. Moreover, there is an observed decrease in the hopping distance (λ) from the hopping conduction fitting results (Supplementary Fig. 22), for instance, the λ decreases from 1.06 for the 3-layered nanolaminate to 0.9 for the 5-layered nanolaminate and further to 0.77 for the 7-layered. This suggests a higher density of traps in the 7-layered and 5-layered nanolaminates compared to the 3-layered counterpart^{47,48}.

The suppressed leakage current density in the 7-layered and 5-layered nanolaminate compared to 3-layered nanolaminate is attributed to the presence of a higher number of PEI/ Al_2O_3 interfaces. The change of PEI configurations in the interfacial area near the Al_2O_3 surface can serve as defects and impurities, which enhances the density of charge traps^{49,50}. An increased number of interfaces in multilayered nanolaminate leads to a higher trap density, resulting in a reduced hopping distance between neighboring traps. Additionally, trapped charges at the interfaces induce a built-in electric field that counteracts the applied electric field, thereby increasing the potential

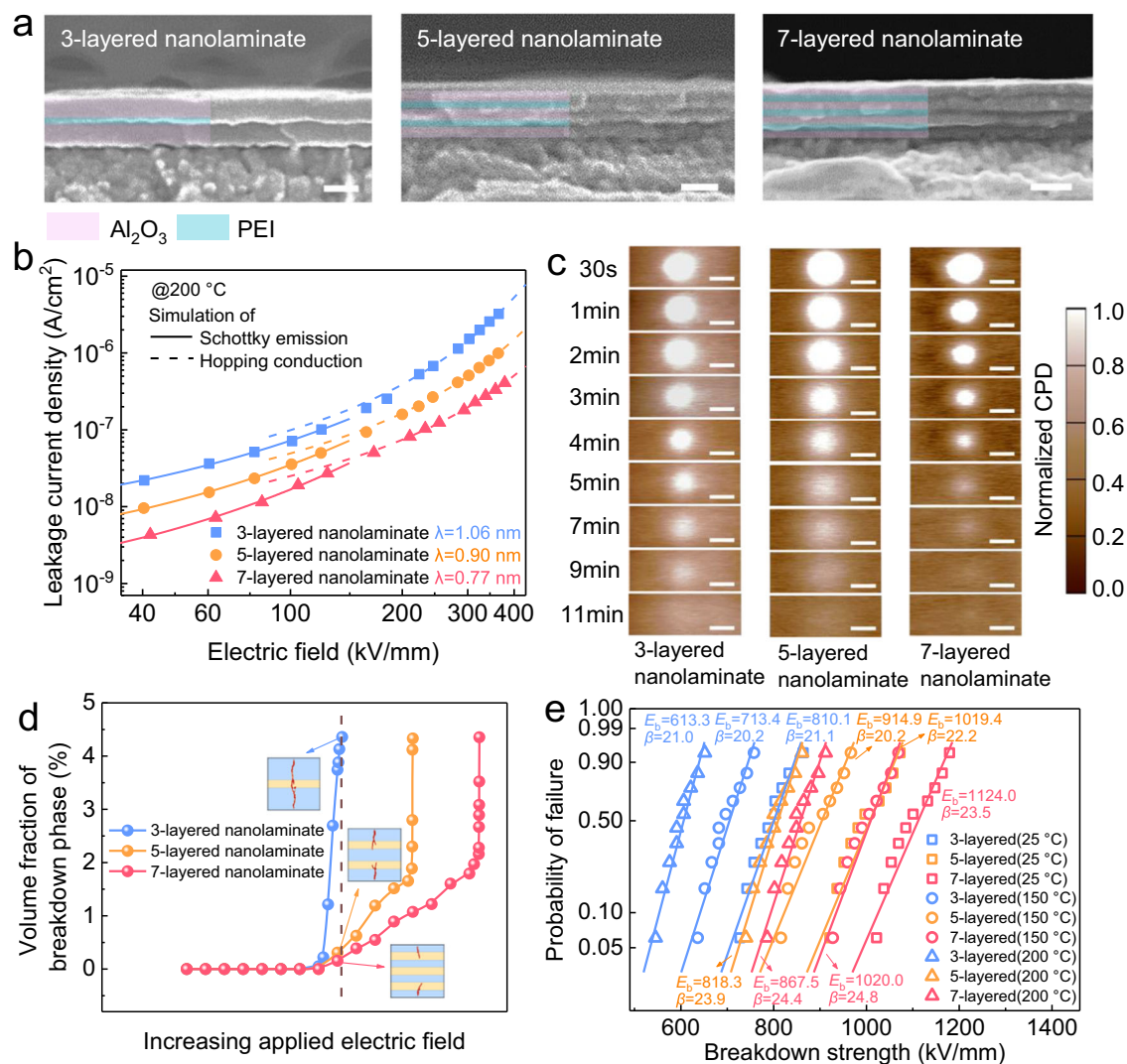


Fig. 2 | Structures and electric properties of multilayered nanolaminates.

a Cross-section SEM images of nanolaminates with varying layers and interlayer PEI thickness of 10 nm. The pink region represents Al_2O_3 , and the blue region represents PEI. The scale bar is 50 nm for all. **b** Leakage current densities of nanolaminates with varying layers as a function of an electric field at 200 °C. **c** KPFM maps of the normalized contact potential difference (CPD) of nanolaminates with varying

layers. From top to bottom, -30 s, -1 min, -2 min, -3 min, -4 min, -5 min, -7 min, -9 min, -11 min after applying a 20 V voltage at the surface of the samples. The scale bar is 1 μm . **d** Simulated evolution of volume fraction of breakdown phase for different multilayered nanolaminates. **e** Failure probability of breakdown strength deduced from Weibull distribution for nanolaminates with varying layers at 25, 150, and 200 °C, respectively.

barrier for charge injection⁵¹. This elevated injection barrier is evidenced by employing Kelvin probe force microscopy (KPFM) to measure surface potential decay after applying a voltage of 20 V (Fig. 2c). The normalized contact potential difference (CPD) of the 7-layered nanolaminate declined rapidly within 7 min, while a longer time is needed for 5-layered and 3-layered counterparts, being 9 and 11 min, respectively. The higher charge dissipation rate in 7-layered nanolaminate is primarily ascribed to the stronger built-in electric field by the presence of more PEI- Al_2O_3 interfaces, which provides a stronger driving force for rapid surface charge dissipation^{19,51}. The impact of interfacial traps on the charge transport behaviors is further elucidated and simulated by a unipolar electron injection transport model^{52,53}. Supplementary Fig. 23 illustrates the simulated local charge distribution and corresponding line profiles, which reveal that the presence of interfacial traps captures charges and results in higher charge density at the PEI/ Al_2O_3 interfaces in these multilayered laminates. Furthermore, compared to 3-layered nanolaminates, the charge transport is delayed in 5-layered and 7-layered nanolaminates, aligning well with the observed experimental leakage currents.

It should be noted that the breakdown of dielectrics is often characterized by the formation of penetrating electrical trees. The presence of PEI- Al_2O_3 interfaces in the multilayered nanolaminates is expected to exert an impact on the path-dependent breakdown process. To investigate this, the propagation process of the breakdown paths under increasing applied electric field in multilayered laminate is visualized by phase-field simulation. The volume fraction of the breakdown phase was calculated to quantitatively determine the occurrence of the breakdown, where a saturated breakdown phase indicates the formation of a penetrating breakdown path⁴⁰. Supplementary Fig. 24 illustrates the real-time evolution of breakdown paths, demonstrating that the breakdown path is driven by the electric field and expands laterally with the formation of branches near the PEI/ Al_2O_3 interface. This impedes its propagation and delays the occurrence of breakdown. Due to the presence of more interfaces, the 7-layered nanolaminate exhibits a slower increase in the volume fraction of the breakdown phase compared to the other two counterparts (Fig. 2d), implying the strongest resistance to breakdown.

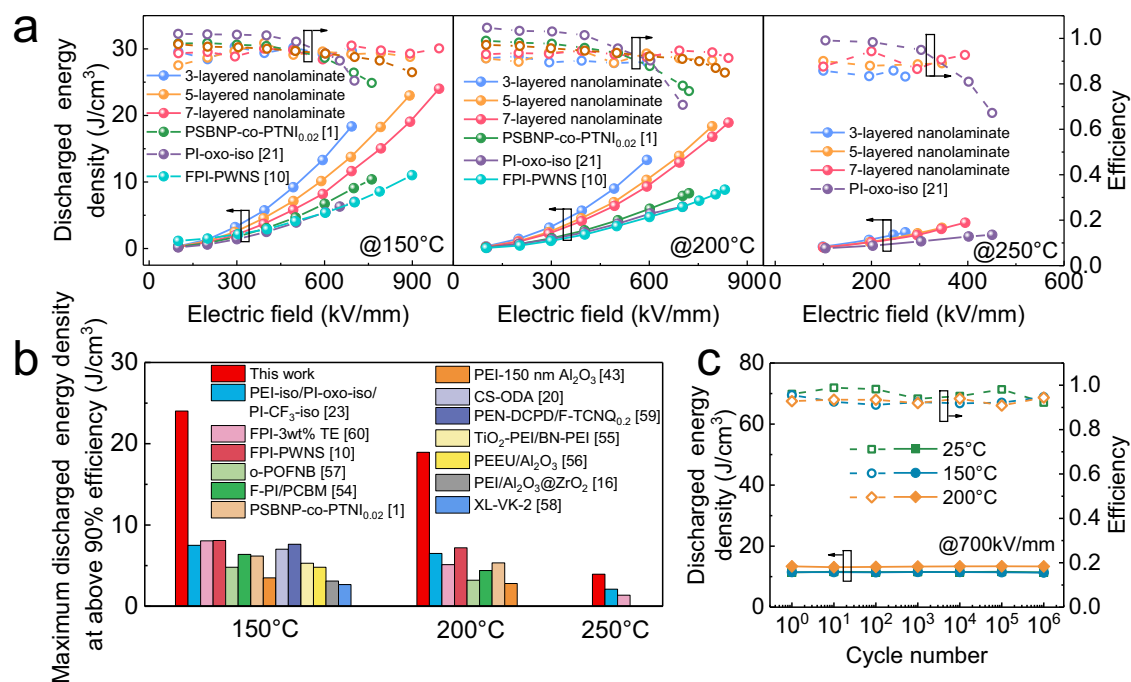


Fig. 3 | Energy storage performance and cyclic properties for multilayered nanolaminates. **a** Discharged energy density and efficiency of nanolaminates with varying layers at temperatures of 150, 200, and 250 °C. **b** Comparison of maximum discharged energy density achieved at above 90% efficiency in this work and

previously reported values at different temperatures. **c** Cyclic stability of energy density and energy efficiency for 7-layered nanolaminate under 700 kV/mm at various temperatures.

The PEI/Al₂O₃ interfaces endow the multilayered nanolaminates with notably reduced high-temperature leakage current and the ability to delay the breakdown path, demonstrating exceptional electrical breakdown properties. As expected, the room temperature breakdown strength of 7-layered nanolaminate reaches up to ~1120 kV/mm, which suggests a ~40% enhancement over that of 3-layered laminate (~810 kV/mm) (Fig. 2e). The high E_b of the 7-layered nanolaminate is maintained with increasing temperature, with values on the orders of 1020 kV/mm and 870 kV/mm at 150 and 200 °C, respectively. Additionally, the Weibull modulus β of all these nanolaminates is between 20 and 30, indicating a narrow distribution of experimental results and excellent reliability.

In addition to breakdown strength, the dielectric constant is another crucial parameter for assessing the energy storage capability of the films. As shown in Supplementary Figs. 25, 26, all the multilayered PEI/Al₂O₃ nanolaminates deliver a higher ϵ_r compared to the pristine PEI (~3.2), due to the Al₂O₃ having an intrinsically higher ϵ_r of 10. A reduction in the dielectric constant with increasing the number of layers within the multilayered laminates is due to the decreasing proportion of Al₂O₃ with the number of layers. All of these nanolaminates exhibit outstanding temperature stability of dielectric properties across a broad temperature range of 25–200 °C, with the dielectric loss maintained at an ultralow level of <0.01.

Energy storage properties of nanolaminates

The high E_b and suppressed high-temperature leakage current at elevated temperatures, together with the minimal variation of the dielectric constant, will greatly benefit the energy storage performance of the multilayered nanolaminate. The U_e and efficiency (η) of the nanolaminates were analyzed according to the electrical displacement (D)–electric field (E) loops (Supplementary Figs. 27, 28). The U_e of the 3-layered nanolaminates was initially investigated with varying thicknesses of PEI. It consistently increases as the thickness of the PEI film decreases, as demonstrated in Supplementary Fig. 29. Importantly, when comparing two 3-layered nanolaminates with

identical proportions of PEI and Al₂O₃ but different PEI thicknesses, the 3-layered nanolaminate with a 10-nm-thick PEI exhibits higher U_e compared to its counterpart with a 40-nm-thick PEI at the same PEI/Al₂O₃ proportion (Supplementary Fig. 30). This further confirms that the enhanced energy density in layered nanolaminates is primarily ascribed to nanoconfinement. Moreover, the 7-layered and 5-layered nanolaminates demonstrate further improved energy storage performances due to an increased number of interfaces, despite a reduced proportion of Al₂O₃ compared to the 3-layered nanolaminate (Supplementary Fig. 31). As shown in Fig. 3a and Supplementary Fig. 32, owing to its exceptional E_b contribution, 7-layered nanolaminate achieves the highest U_e of all studied films, with a maximum value of 29.5 J/cm³ at a field of 1090 kV/mm at 25 °C. In comparison, the 5-layered nanolaminate has a value of 27.1 J/cm³ at a field of 990 kV/mm and the 3-layered nanolaminate exhibits a value of 22.4 J/cm³ at a field of 790 kV/mm. Remarkably, at elevated temperatures, the 7-layered nanolaminate still exhibits a high U_e , with values of 24.0 J/cm³ at 150 °C, 18.9 J/cm³ at 200 °C, and 3.9 J/cm³ at 250 °C. Of particular importance is that a high energy efficiency of >90% is maintained over the entire temperature range up to 250 °C, due to the superior thermal-electrical stability and suppressed leakage current. The multilayered nanolaminates consistently exhibit the highest U_e among all the extensively studied flexible dielectrics at temperatures of 150 and 200 °C (Fig. 3b)^{1,10,16,20,23,43,54–60}. Even at temperatures as high as 250 °C where most polymeric dielectrics fail to operate, the 7-layered laminate still achieves a high U_e of 3.9 J/cm³ at an electric field of 400 kV/mm, which is approximately twice that of the best-performing PI-oxo-iso (~2.1 J/cm³ at η ~90%)²³. From a practical application viewpoint, the multilayered nanolaminate undergoes a cyclic charging-discharging test at a high electric field of 700 kV/mm under different temperatures to assess its reliability. The cyclic energy storage properties are given in Fig. 3c, where both the discharged energy density and efficiency are found to remain the same values across different temperatures even after 10⁶ consecutive cycles, demonstrating excellent cyclic reliability of the energy storage performance. The multilayered nanolaminates

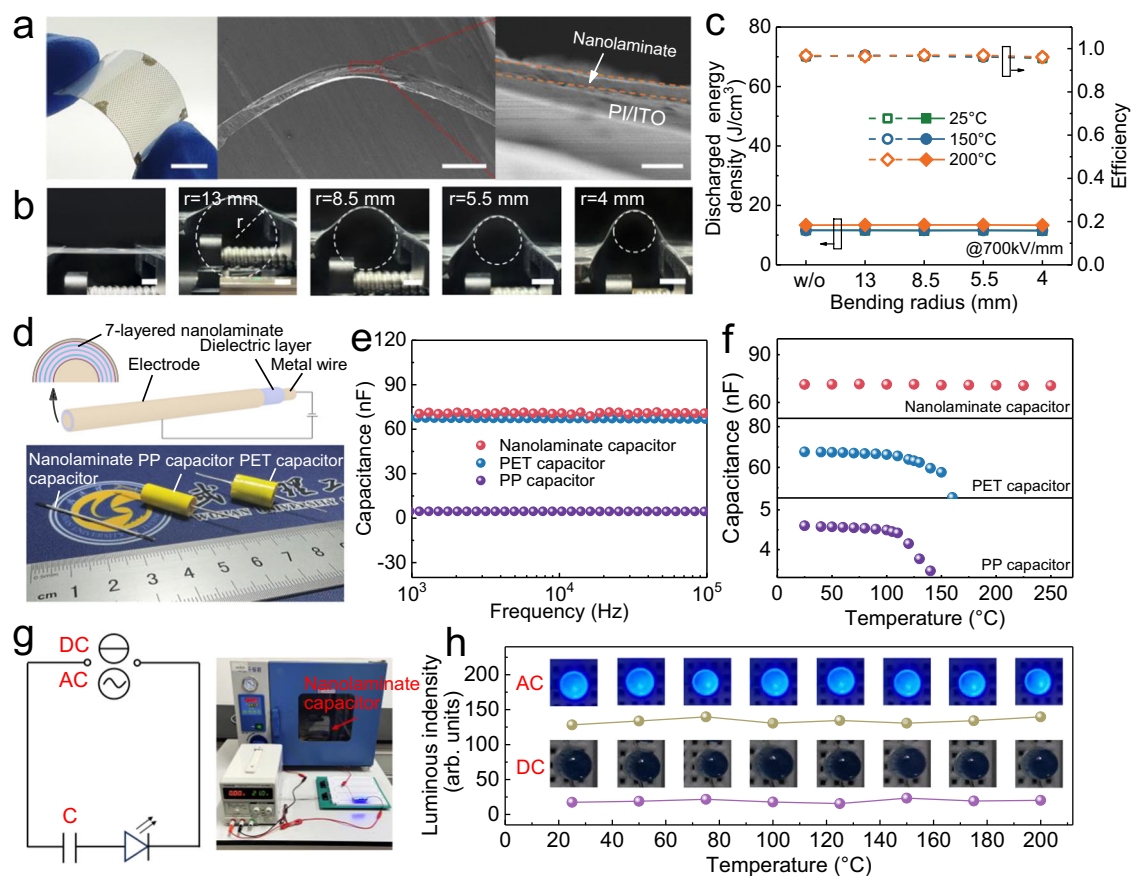


Fig. 4 | Evaluation of the nanolaminate flexibility and the metal-wire-based capacitor device. **a** Optical photograph (left) of 7-layered nanolaminate on a flexible substrate and the cross-sectional SEM images of the nanolaminate under bending deformation (middle), the right is the partially enlarged image. The scale bar is 1 cm in the left image, 400 μm in the middle image, and 200 nm in the right image. **b** The front view of the device bent at different bending radius. The scale bar is 5 mm for all. **c** Discharged energy density and efficiency as a function of varying bending radius (13, 8.5, 5.5, 4 mm) after 1000 cycles of bending. **d** Schematic

diagram of the metal-wire based nanolaminate capacitor and the optical photograph, comparing with commercial metallized PP and PET capacitors. **e**, **f** The capacitance of metal-wire-based nanolaminate capacitors compared with commercial metallized PP and PET capacitors as a function of **e** frequency and **f** temperature. **g** Electric circuit schematic and physical implementation of capacitors operating in circuits with AC and DC voltage sources. **h** Luminous intensity of LEDs in circuits with AC voltage source and DC voltage source under varying temperatures, the inset is the top view of the brightness of LEDs.

also demonstrate remarkable thermal cycling stability as evidenced by the unchanged discharged energy density and efficiency values after undergoing 100 thermal cycles between 25 to 200 °C (Supplementary Fig. 33). Additionally, the outstanding energy storage performances of the nanolaminates showcase excellent resistance to aging and humidity, suggesting long-term stability and reliability in practical applications (Supplementary Figs. 34, 35).

It is interesting to note that the studied multilayered PEI/Al₂O₃ nanolaminate also exhibits high flexibility. The cross-sectional SEM images presented in Fig. 4a demonstrate the multilayered nanolaminate retains its structural integrity under a bending deformation, exhibiting no signs of damage. In the bending test, the 7-layered nanolaminate with polyimide (PI) substrate was bent with varying bending radii of 4, 5.5, 8.5, and 13 mm (Fig. 4b) and then recovered up to 1000 times, indicating its exceptional flexibility. Figure 4c and Supplementary Fig. 36 showcase the bending radius dependence of energy density and efficiency for 7-layered nanolaminate measured after 1000 consecutive bendings, the laminate at different bending radii delivers consistent values of energy density and energy efficiency across the temperature range of 25 to 250 °C. As shown in Supplementary Figs. 37, 38, at the maximum degree of bending radius of 4 mm, the energy density and efficiency at various temperatures show no signs of degradation after 1000 consecutive bendings. Of particular significance is that the nanolaminate can be attached to a curved

surface beyond the traditional flat plane. The distinctive feature of this property has inspired the development of a metal-wire-based nanolaminate capacitor, which is characterized by its simplicity and ease of fabrication, as well as its exceptional efficiency and seamless integration capabilities. Figure 4d illustrates the capacitor, which features a metal wire serving as the inner electrode and substrate of the nanolaminate. The 7-layered nanolaminate, as seen in Supplementary Fig. 39, is attached to the metal wire surface to function as a dielectric layer, followed by the deposition of an outer Pt electrode. The capacitor utilizing the ultrathin nanometer-scale laminate delivers a high capacitance of ~70 nF across a frequency range of 1–100 kHz (Fig. 4e). Despite having a small device size that is similar to the pristine metal wire (diameter of 0.8 mm, ϕ 0.8 mm), it exhibits superior capacitance compared to commercial metallized polypropylene film (PP, 5 nF, ϕ 8 mm) and commercial metallized polyethylene terephthalate film (PET, 68 nF, ϕ 8.7 mm) capacitors. It is worth mentioning that the metal-wire nanolaminate capacitor also demonstrates excellent temperature stability, with its capacitance remaining the same across the temperature range of 25–250 °C, while the commercial PP and PET capacitors experience a decline in capacitance beyond 100 °C (Fig. 4f). To showcase the practical application of the metal-wire nanolaminate capacitors, we employ the capacitor as the energy storage component to power and illuminate light-emitting diodes (LEDs) in the electronic circuit (Fig. 4g). As shown in Fig. 4h, the charge-discharge process of

the nanolaminate capacitor under the AC power generates current to illuminate the LEDs. In contrast, the insulating capacitor prevents current flow under DC power, resulting in non-illuminated LEDs. Notably, even when the nanolaminate capacitor is heated up to 200 °C, the luminous intensity of the LEDs in the AC circuit remains consistent, whereas the LEDs in the DC circuit remain off, highlighting the exceptional thermal stability of the metal-wire nanolaminate capacitor device.

Discussion

Our study underscores the potential of multilayered polymer nanolaminates incorporating nanoconfined polymer ultrathin films for high-temperature dielectric energy storage applications. The highly flexible Al₂O₃-PEI nanolaminate, incorporating 10-nm-thick nanoconfined PEI ultrathin films, produces a high U_e of 24.0 J/cm³ at 150 °C, 18.9 J/cm³ at 200 °C, and 3.9 J/cm³ at 250 °C, while maintaining a high energy efficiency of >90% across the entire temperature range, with excellent charging-discharging reliability up to 10⁶ at various temperatures. While large-scale production of nanolaminates using alternating spin-coating and ALD procedures may be challenging at present, the synergistic effect of nanoconfinement and interfaces in multilayered nanolaminates offers a promising strategy, which can be used for the development of high-performance polymer-ceramic composite systems with exceptional high-temperature stability while retaining superior flexibility and performance.

Methods

Sample preparation

PI films coated with indium tin oxide (ITO) were employed as flexible deposition substrates with high-temperature resistance. Al₂O₃ nanolayers were deposited by plasma-enhanced ALD (PEALD) with a GEM-STAR benchtop ALD system with Trimethylaluminum [TMA, Al(CH₃)₃] as a precursor. The bottom Al₂O₃ nanolayer on the ITO/PI substrate was deposited under 300 m Torr at 130 °C. Each deposition cycle consisted of TMA pulse/argon purging/oxygen plasma pulse/argon purging, with respective durations of 22 ms, 5 s, 10 s, and 5 s. The thickness of the Al₂O₃ nanolayers was precisely controlled by manipulating the number of deposition cycles, whereby a single cycle yields an Al₂O₃ nanolayer with a precise thickness of 0.14 nm. For the preparation of the PEI nanofilm, PEI pellets (purchased from SABIC Innovative Plastics) were dissolved in *N*-methyl pyrrolidone (NMP, purchased from Aladdin), and stirred at 50 °C for 24 h. The PEI nanofilm was then prepared by spin-coating, and the thickness of the polymer film was controlled by solution concentration and the rotational speed of the spin-coating. For PEI with thicknesses of 10, 40, 165, 360, 720 nm, and 1.3 μm, the corresponding solution concentrations and spin-coating speeds were as follows: 2 wt% and 8000 rpm, 4 wt% and 8000 rpm, 10 wt% and 8000 rpm, 10 wt% and 3000 rpm, 15 wt% and 3000 rpm, 20 wt% and 3000 rpm, respectively. Before the next preparation of the top Al₂O₃ nanolayer, the PEI nanofilm was dried in a vacuum oven at 70 °C for 24 h to remove residual solvent. The top Al₂O₃ nanolayer was deposited with the same process as the bottom Al₂O₃ nanolayer. The multilayered nanolaminates, as required, were obtained by alternating ALD and spin-coating processes. The trilayered PEI-Al₂O₃ nanolaminate was also fabricated on a silicon wafer substrate using the same procedures, in order to measure T_g and Young's modulus.

Structure and AFM-based characterization

The cross-sectional morphology of multilayer structured nanolaminates was characterized with scanning electron microscopy (JSM-7610FPlus, JEOL, Japan). The characterization of thickness, T_g , and Young's modulus of PEI film with different thicknesses was implemented on a commercial atomic force microscope AFM (Cypher ES, Asylum Research, USA). The thickness is determined by steps height

difference between the PEI layer and the substrate as shown in Supplementary Fig. 2. A Si cantilever with Al reflective coating layer of spring constant 2 N m⁻¹ (Asylum Research ASYELEC-01-R2) was utilized. The trilayered nanocomposite Al₂O₃ (28 nm)/PEI/Al₂O₃ (1 nm) was prepared for the mechanical tests, with the top layer of Al₂O₃ precisely controlled to a thickness of 1 nm. This ensures a robust interface while allowing for deformation under the pressure exerted by an AFM indenter. Kelvin probe force microscope (KPFM) was employed to test the surface potential of the laminate in KPFM mode after applying a 20 V voltage.

Measurements of electric properties

Before electrical measurements, Pt electrodes were sputtered on the surface of nanolaminates, while the PI/ITO substrate was utilized as the bottom electrode with ITO coating (Supplementary Fig. 40). The thickness of Pt electrodes is 50 nm, and their diameter varies for nanolaminates with different PEI polymer thicknesses: 200 μm for 10 nm PEI, 300 μm for 40 nm PEI, 500 μm for 165 nm and 360 nm PEI, 1 mm for 720 nm PEI, 2 mm for 1.3 μm PEI. Displacement–electric (D – E) field hysteresis loops at different temperatures were recorded at 100 Hz by a multiferroic ferroelectric test system (Premier II, Radiant Technologies, Inc.). The DC leakage current densities (in A cm⁻²) were also calculated by $\nabla D \cdot \text{Area} / \nabla t$ with this ferroelectric test system. Electric breakdown strength tests were performed with a withstand voltage test system (6517B high resistance meter) at a ramping rate and 2 V/s with a limit current of 5 mA.

Molecular dynamics simulations

All the simulations were performed using Materials Studio with the COMPASS II force field⁶¹, which has been used to accurately and simultaneously describe the intra- and inter-molecular interactions for many inorganics and polymers. About 50 PEI molecular chains with each of four monomers were constructed from the Al₂O₃ nanolayer with an initial density of 1.25 g/cm³. The dimensions of the simulation box are $a = 49.457 \text{ \AA}$, $b = 47.590 \text{ \AA}$, and $c = 92.364 \text{ \AA}$. The periodic lattice of the Al₂O₃ nanolayer was fixed at its lattice positions, interacting with the PEI chains only via van der Waals and electrostatic interactions. The amorphous cell[®] module was used to construct the PEI-Al₂O₃ composite unit cell. Forcite module[®] was used for geometry optimization via the conjugate gradient method and annealing with the isothermal (NVT) ensemble for preparing energetically minimized unit cell structure. Then the system was followed by 500-ps production runs in the NVT ensemble at various temperatures, ranging from 300 to 550 K with an interval of 25 K using the Noé-Hoover thermostat with a time step of 1 fs. The non-bonded van der Waals interactions were cut off at 12.5 Å and periodic boundary conditions were applied in all three dimensions. The molecular trajectory diagram was obtained from the two atoms forming the C-H bond in PEI configuration, and each system contains 100 samples with an interval of 5 ps.

The mean-square displacement (MSD) is defined by

$$\text{MSD} = \frac{1}{N} \left\langle \sum_{i=1}^N |r_i^c(t) - r_i^c(0)|^2 \right\rangle \quad (1)$$

where $r_i^c(t)$ is the location of the atom i at time t . The self-diffusion coefficient can also be obtained from the long-time limit of the MSD using the well-known Einstein relation⁶²

$$D_i = \frac{1}{6} \lim_{t \rightarrow \infty} \frac{d}{dt} \left\langle |r_i^c(t) - r_i^c(0)|^2 \right\rangle \quad (2)$$

Phase-field simulation

A modified stochastic model for dielectric breakdown was employed to simulate the developing process of electrical trees in multilayer

nanocomposite films, based on the framework proposed by ref. 63. In this model, the breakdown probability of local points is defined to be dependent on the local electric field, which can be described as

$$P_{\text{breakdown}}(\mathbf{r}) = \frac{E(\mathbf{r})}{E_b(\mathbf{r})} \quad (3)$$

where $E(\mathbf{r})$ is the local electric field, and $E_b(\mathbf{r})$ is the intrinsic breakdown of the material. Then, the local electric field distribution can be obtained by solving the electrostatic Poisson's equation,

$$\nabla \cdot (\varepsilon_0 \varepsilon_r E) = \rho_V \quad (4)$$

$$E = -\nabla V \quad (5)$$

where ε_0 is the vacuum dielectric constant, ε_r is the relative dielectric constant, ρ_V is the space charge density, and V is the electric potential, respectively.

The impact of interfacial traps on the charge transport behaviors is elucidated by a unipolar electron injection transport model^{52,53}. In this model, the process of charge injection is described using the Schottky injection mechanism, while the migration of electrons in polymer nanocomposites is characterized by a set of equations including the transport equation, continuity equation, and Poisson's equation.

Based on the Schottky injection mechanism, the electron injection process at the interface between the dielectric and the electrode is described by,

$$J = AT^2 \exp\left(-\frac{\varphi_i}{k_B T}\right) \exp\left(\frac{e}{k_B T} \sqrt{\frac{eE(\mathbf{r}, t)}{4\pi\varepsilon_0\varepsilon_r}}\right) \quad (6)$$

where J the current density, A the Richardson constant, T the temperature, φ_i the injection potential barrier, k_B the Boltzmann constant, e the elementary charge, E the electric field, ε_0 the vacuum permittivity, ε_r the relative permittivity, respectively. The electron migration process in polymer nanocomposites is described by the transport equation, continuity equation, and Poisson's equation as follows,

$$\nabla(\varepsilon_0 \varepsilon_r (E(\mathbf{r}, t))) = n(\mathbf{r}, t) \quad (7)$$

$$J(\mathbf{r}, t) = \mu_a(\mathbf{r}, t) n(\mathbf{r}, t) E(\mathbf{r}, t) \quad (8)$$

$$\frac{\partial n(\mathbf{r}, t)}{\partial t} + \frac{\partial J(\mathbf{r}, t)}{\partial \mathbf{r}} = s \quad (9)$$

where n is the charge density and s is the source term ($s = 0$ in this simulation). The apparent mobility μ_a is introduced to describe the trapping or detrapping process of mobile electrons at the interface regions between the PEI and Al_2O_3 , which could be written by,

$$\mu_a = \mu_0 \exp\left(\frac{-\varphi_a}{k_B T}\right) \quad (10)$$

The parameters used in this simulation are given in Supplementary Table 1.

The construction of a metal-wire-based nanolaminate capacitor device

Based on a Cu wire with a diameter of 0.8 mm as an inner electrode, 7-layered PEI- Al_2O_3 nanolaminate was deposited on the surface by ALD and spin-coating. The outer Pt electrode with a thickness of 50 nm was coated by a JEC-3000FC ion sputter device (JEOL, Japan). The

capacitance of the capacitor device was measured with a precision impedance analyzer (4294A, Agilent, USA) at different temperatures.

Data availability

The data that support the findings of this study are available within the article and its Supplementary Information/Source Data file, and also from the corresponding author upon request. Source data are provided with this paper.

References

- Chen, J. et al. Ladderphane copolymers for high-temperature capacitive energy storage. *Nature* **615**, 62–66 (2023).
- Kim, J. et al. Ultrahigh capacitive energy density in ion-bombarded relaxor ferroelectric films. *Science* **369**, 81–84 (2020).
- Chu, B. et al. A dielectric polymer with high electric energy density and fast discharge speed. *Science* **313**, 334–336 (2006).
- Pan, H. et al. Ultrahigh-energy density lead-free dielectric films via polymorphic nanodomain design. *Science* **365**, 578–582 (2019).
- Yang, B. et al. Engineering relaxors by entropy for high energy storage performance. *Nat. Energy* **8**, 956–964 (2023).
- Yang, B. et al. High-entropy enhanced capacitive energy storage. *Nat. Mater.* **21**, 1074–1080 (2022).
- Li, Q. et al. Flexible high-temperature dielectric materials from polymer nanocomposites. *Nature* **523**, 576–579 (2015).
- Watson, J. & Castro, G. A review of high-temperature electronics technology and applications. *J. Mater. Sci. Mater. Electron.* **26**, 9226–9235 (2015).
- Buttay, C. et al. State of the art of high temperature power electronics. *Mater. Sci. Eng. B* **176**, 283–288 (2011).
- Yang, M. et al. Roll-to-roll fabricated polymer composites filled with subnanosheets exhibiting high energy density and cyclic stability at 200 °C. *Nat. Energy* <https://doi.org/10.1038/s41560-023-01416-3> (2024).
- Zhang, X. et al. Giant energy density and improved discharge efficiency of solution-processed polymer nanocomposites for dielectric energy storage. *Adv. Mater.* **28**, 2055–2061 (2016).
- Li, H. et al. Dielectric polymers for high-temperature capacitive energy storage. *Chem. Soc. Rev.* **50**, 6369–6400 (2021).
- Tan, D., Zhang, L., Chen, Q. & Irwin, P. High-temperature capacitor polymer films. *J. Electron. Mater.* **43**, 4569–4575 (2014).
- Liu, X.-J., Zheng, M.-S., Chen, G., Dang, Z.-M. & Zha, J.-W. High-temperature polyimide dielectric materials for energy storage: theory, design, preparation and properties. *Energy Environ. Sci.* **15**, 56–81 (2022).
- Yang, M. et al. Polymer nanocomposite dielectrics for capacitive energy storage. *Nat. Nanotechnol.* <https://doi.org/10.1038/s41565-023-01541-w> (2024).
- Ren, L. et al. High-temperature high-energy-density dielectric polymer nanocomposites utilizing inorganic core-shell nanostructured nanofillers. *Adv. Energy Mater.* **11**, 2101297 (2021).
- Zhou, Y. et al. A scalable, high-throughput, and environmentally benign approach to polymer dielectrics exhibiting significantly improved capacitive performance at high temperatures. *Adv. Mater.* **30**, 1805672 (2018).
- Dai, Z. et al. Scalable polyimide-poly(amic acid) copolymer based nanocomposites for high-temperature capacitive energy storage. *Adv. Mater.* **34**, 2101976 (2022).
- Yuan, C. et al. Polymer/molecular semiconductor all-organic composites for high-temperature dielectric energy storage. *Nat. Commun.* **11**, 3919 (2020).
- Pan, Z. et al. Tailoring poly(styrene-co-maleic anhydride) networks for all-polymer dielectrics exhibiting ultrahigh energy density and charge-discharge efficiency at elevated temperatures. *Adv. Mater.* **35**, 2207580 (2023).

21. Zhang, B. et al. Superior high-temperature energy density in molecular semiconductor/polymer all-organic composites. *Adv. Funct. Mater.* **33**, 2210050 (2023).
22. Zhang, Q. et al. High-temperature polymers with record-high breakdown strength enabled by rationally designed chain-packing behavior in blends. *Matter* **4**, 2448–2459 (2021).
23. Wang, R. et al. Designing tailored combinations of structural units in polymer dielectrics for high-temperature capacitive energy storage. *Nat. Commun.* **14**, 2406 (2023).
24. Yang, M. et al. Quantum size effect to induce colossal high-temperature energy storage density and efficiency in polymer/inorganic cluster composites. *Adv. Mater.* **35**, 2301936 (2023).
25. Zuo, B., Zhou, H., Davis, M. J. B., Wang, X. & Priestley, R. D. Effect of local chain conformation in adsorbed nanolayers on confined polymer molecular mobility. *Phys. Rev. Lett.* **122**, 217801 (2019).
26. Oh, H. & Green, P. F. Polymer chain dynamics and glass transition in athermal polymer/nanoparticle mixtures. *Nat. Mater.* **8**, 139–143 (2009).
27. Papon, A. et al. Glass-transition temperature gradient in nanocomposites: evidence from nuclear magnetic resonance and differential scanning calorimetry. *Phys. Rev. Lett.* **108**, 065702 (2012).
28. Ellison, C. J. & Torkelson, J. M. The distribution of glass-transition temperatures in nanoscopically confined glass formers. *Nat. Mater.* **2**, 695–700 (2003).
29. Ediger, M. D. & Forrest, J. A. Dynamics near free surfaces and the glass transition in thin polymer films: a view to the future. *Macromolecules* **47**, 471–478 (2014).
30. Rittigstein, P., Priestley, R. D., Broadbelt, L. J. & Torkelson, J. M. Model polymer nanocomposites provide an understanding of confinement effects in real nanocomposites. *Nat. Mater.* **6**, 278–282 (2007).
31. Yang, J.-L. et al. Dielectric-metallic double-gradient composition design for stable Zn metal anodes. *ACS Energy Lett.* **8**, 2042–2050 (2023).
32. Lv, J. et al. Microstructure evolution and interfacial bonding mechanisms of ultrasonically soldered sapphire/Al dissimilar joints using Sn-based solders. *Ceram. Int.* **48**, 20070–20077 (2022).
33. Zhang, H., Sun, D.-D., Peng, Y., Huang, J.-H. & Luo, M.-B. Diffusivity and glass transition of polymer chains in polymer nanocomposites. *Phys. Chem. Chem. Phys.* **21**, 23209–23216 (2019).
34. El Magri, A. & Vaudreuil, S. Effects of physical and chemical ageing on 3D printed poly (ether ether ketone)/poly (ether imide) [PEEK/PEI] blend for aerospace applications. *J. Mater. Sci.* **58**, 1465–1479 (2023).
35. Brunner, R., Etsion, I. & Talke, F. E. A simple atomic force microscopy calibration method for direct measurement of surface energy on nanostructured surfaces covered with molecularly thin liquid films. *Rev. Sci. Instrum.* **80**, 055109 (2009).
36. Krieg, M. et al. Atomic force microscopy-based mechanobiology. *Nat. Rev. Phys.* **1**, 41–57 (2018).
37. Liu, Y., Sokolov, I., Dokukin, M. E., Xiong, Y. & Peng, P. Can AFM be used to measure absolute values of Young's modulus of nanocomposite materials down to the nanoscale? *Nanoscale* **12**, 12432–12443 (2020).
38. Stark, K. H. & Garton, C. G. Electric strength of irradiated polythene. *Nature* **176**, 1225 (1955).
39. Zhang, X. et al. Polymer nanocomposites with ultrahigh energy density and high discharge efficiency by modulating their nanostructures in three dimensions. *Adv. Mater.* **30**, 1707269 (2018).
40. Jiang, Y. et al. Ultrahigh energy density in continuously gradient-structured all-organic dielectric polymer films. *Adv. Funct. Mater.* **32**, 2200848 (2022).
41. Shen, Z.-H. et al. Phase-field modeling and machine learning of electric-thermal-mechanical breakdown of polymer-based dielectrics. *Nat. Commun.* **10**, 1843 (2019).
42. Meng, N. et al. Ultrahigh β -phase content poly(vinylidene fluoride) with relaxor-like ferroelectricity for high energy density capacitors. *Nat. Commun.* **10**, 4535 (2019).
43. Cheng, S. et al. Polymer dielectrics sandwiched by medium-dielectric-constant nanoscale deposition layers for high-temperature capacitive energy storage. *Energy Storage Mater.* **42**, 445–453 (2021).
44. Li, X. et al. Unraveling bilayer interfacial features and their effects in polar polymer nanocomposites. *Nat. Commun.* **14**, 5707 (2023).
45. Zhang, X. et al. Superior energy storage performances of polymer nanocomposites via modification of filler/polymer interfaces. *Adv. Mater. Interfaces* **5**, 1800096 (2018).
46. Calvet, L. E., Wheeler, R. G. & Reed, M. A. Electron transport measurements of Schottky barrier inhomogeneities. *Appl. Phys. Lett.* **80**, 1761–1763 (2002).
47. Chiu, F.-C. A review on conduction mechanisms in dielectric films. *Adv. Mater. Sci. Eng.* **2014**, 1–18 (2014).
48. Ambegaokar, V., Halperin, B. I. & Langer, J. S. Hopping conductivity in disordered systems. *Phys. Rev. B* **4**, 2612–2620 (1971).
49. Tanaka, T. Dielectric nanocomposites with insulating properties. *IEEE Trans. Dielectr. Electr. Insul.* **12**, 914–928 (2005).
50. Donzel, L. & Schuderer, J. Nonlinear resistive electric field control for power electronic modules. *IEEE Trans. Dielectr. Electr. Insul.* **19**, 955–959 (2012).
51. Li, H. et al. High-performing polysulfate dielectrics for electrostatic energy storage under harsh conditions. *Joule* **7**, 95–111 (2023).
52. Min, D. & Li, S. A comparison of numerical methods for charge transport simulation in insulating materials. *IEEE Trans. Dielectr. Electr. Insul.* **20**, 955–964 (2013).
53. Alison, J. M. & Hill, R. M. A model for bipolar charge transport, trapping and recombination in degassed crosslinked polyethylene. *J. Phys. D Appl. Phys.* **27**, 1291–1299 (1994).
54. Ren, W. et al. Scalable ultrathin all-organic polymer dielectric films for high-temperature capacitive energy storage. *Adv. Mater.* **34**, 2207421 (2022).
55. Wang, P. et al. Ultrahigh energy storage performance of layered polymer nanocomposites over a broad temperature range. *Adv. Mater.* **33**, 2103338 (2021).
56. Zhang, T. et al. A highly scalable dielectric metamaterial with superior capacitor performance over a broad temperature. *Sci. Adv.* **6**, eaax6622 (2020).
57. Deshmukh, A. A. et al. Flexible polyolefin dielectric by strategic design of organic modules for harsh condition electrification. *Energy Environ. Sci.* **15**, 1307–1314 (2022).
58. Li, H. et al. Crosslinked fluoropolymers exhibiting superior high-temperature energy density and charge-discharge efficiency. *Energy Environ. Sci.* **13**, 1279–1286 (2020).
59. Chen, J. et al. Aromatic-free polymers based all-organic dielectrics with breakdown self-healing for high-temperature capacitive energy storage. *Adv. Mater.* **35**, 2306562 (2023).
60. Yang, M., Zhou, L., Li, X., Ren, W. & Shen, Y. Polyimides physically crosslinked by aromatic molecules exhibit ultrahigh energy density at 200 °C. *Adv. Mater.* **35**, 2302392 (2023).
61. Sun, H. et al. COMPASS II: extended coverage for polymer and drug-like molecule databases. *J. Mol. Model.* **22**, 47 (2016).
62. Zhang, X. et al. Atomic simulation of melting and surface segregation of ternary Fe-Ni-Cr nanoparticles. *Appl. Surf. Sci.* **465**, 871–879 (2019).
63. Niemeyer, L., Pietronero, L. & Wiesmann, H. J. Fractal dimension of dielectric breakdown. *Phys. Rev. Lett.* **52**, 1033–1036 (1984).

Acknowledgements

X.Z. was supported by the National Key Research & Development Program of China (Grant No. 2021YFB3800603). C.-W.N. was supported by the Basic Science Center Program of the National Natural Science

Foundation of China (Grant No. 52388201). X.Z. was supported by the National Natural Science Foundation of China (Grant No. 52222205 and 52072280).

Author contributions

X. Zhang and C.-W.N. conceived the idea, designed the research, and supervised the project; X.L. prepared the laminate samples; X.L. performed the structural characterizations and dielectric measurements with assistance from X. Zhen, J. Zhi, and J. Zou; X.L. and S.L. fabricated the capacitor device; B. Liu and B. Li performed the MD simulations; J.W. and Z.S. performed the phase-field simulations; X. Zhang, X. Li, C.-W.N., and S.Z. analyzed the data and wrote the manuscript with input from all authors.

Competing interests

The authors declare no competing interests.

Additional information

Supplementary information The online version contains supplementary material available at <https://doi.org/10.1038/s41467-024-51052-y>.

Correspondence and requests for materials should be addressed to Xin Zhang, Shujun Zhang or Ce-Wen Nan.

Peer review information *Nature Communications* thanks the anonymous reviewer(s) for their contribution to the peer review of this work. A peer review file is available.

Reprints and permissions information is available at <http://www.nature.com/reprints>

Publisher's note Springer Nature remains neutral with regard to jurisdictional claims in published maps and institutional affiliations.

Open Access This article is licensed under a Creative Commons Attribution-NonCommercial-NoDerivatives 4.0 International License, which permits any non-commercial use, sharing, distribution and reproduction in any medium or format, as long as you give appropriate credit to the original author(s) and the source, provide a link to the Creative Commons licence, and indicate if you modified the licensed material. You do not have permission under this licence to share adapted material derived from this article or parts of it. The images or other third party material in this article are included in the article's Creative Commons licence, unless indicated otherwise in a credit line to the material. If material is not included in the article's Creative Commons licence and your intended use is not permitted by statutory regulation or exceeds the permitted use, you will need to obtain permission directly from the copyright holder. To view a copy of this licence, visit <http://creativecommons.org/licenses/by-nc-nd/4.0/>.

© The Author(s) 2024